14 Application of the final design of the dual thin film probe for total temperature measurements downstream the rotor and the second stator of the Brite turbine

14.1 Introduction

One of the main applications of the dual thin film probe is in the VKI Isentropic Light Piston CT3 facility. The time-averaged and the time-resolved components of the gas temperature were successfully measured behind the rotor and behind the second stator of the one and a half stage turbine at *50%* of the blade height. A reference thermocouple was also placed at an angular position of *100°* from the probe and the two measurement technique results were compared.

14.2 Test Conditions, probe design, signal acquisition and calibration

Measurements are performed in the VKI Isentropic Light Piston Compression Tube facility CT3 (Sieverding and Arts, 1992). This facility also simulates aero-engine operating conditions, as the VKI CT2 facility. The test section of CT3 facility is a one and a half stage turbine (Brite turbine) and total temperature measurements are carried out behind the rotor and behind the second stator. The dual thin film probe is fixed between two blades at *50%* of the blade height. A reference thermocouple is also placed at an angular position of *100°* for time-averaged gas temperature measurements. The time-resolved component behind the rotor is also monitored by a reference cold wire probe. Prior to the blowdown, the rotor is brought almost up to the design speed (*6500 RPM*). The nominal operating conditions for these set of experiments are shown in Table 14-1.

T_{01} [K]	P_{01} [bars]	P_{01} / P_{03}	M_3	M_3^{REL}	M_4
475	2.25	3.05	0.42	0.8	0.68

Table 14-1: Operating conditions in CT3

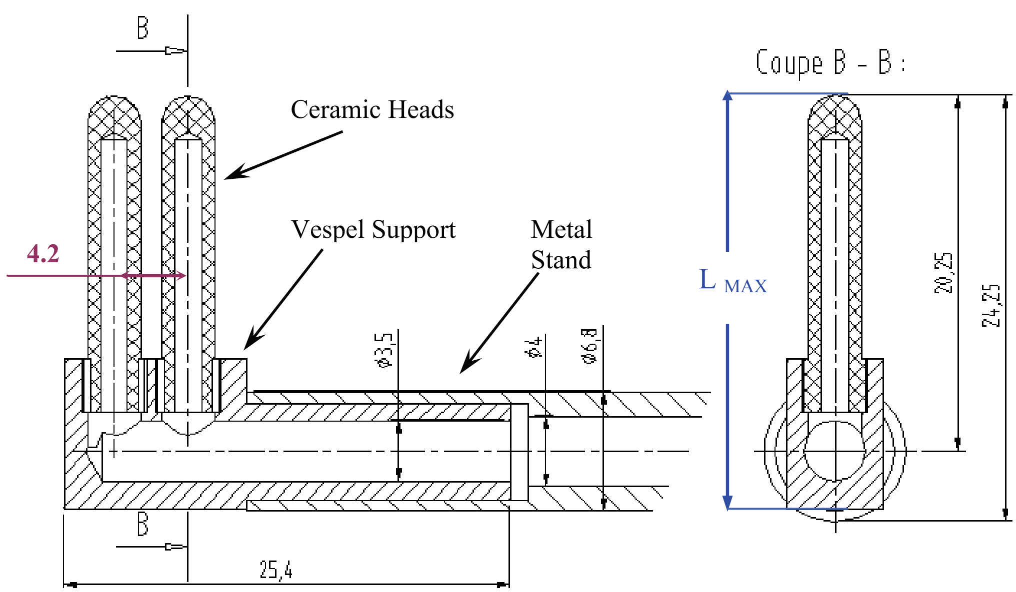

Figure 14-1: New design of the D.T.F.P. for the CT3 tests (all dimensions in mm)

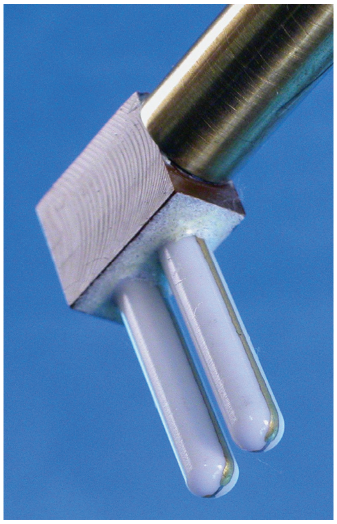

Figure 14-2: The dual thin film probe used for the CT3 measurements (L_{MAX} = 23.5mm)

Gauge CT3 behind the rotor	Resistance Thermometer	Wheatstone Bridge
Hot	T_{W1} = 6.6449 R_1 - 433.39	$d_{\Delta R}/d_{\Delta V}$ = 2.1478 R_0 = (V_0 + 0.0454) / 0.0097
Cold	T_{W2} = 9.849 R_2 - 432.5	$d_{\Delta R}/d_{\Delta V}$ = 2.11 R_0 = (V_0 + 0.0492) / 0.0098
Gauge CT3 behind the second stator	Resistance Thermometer	Wheatstone Bridge
Hot	T_{W1} = 8.7581 R_1 - 405.77	$d_{\Delta R}/d_{\Delta V}$ = 2.11 R_0 = (V_0 + 0.0301) / 0.0096
Cold	T_{W2} = 8.5008 R_2 - 419.44	$d_{\Delta R}/d_{\Delta V}$ = 2.1478 R_0 = (V_0 + 0.0006) / 0.0087

Table 14-2: Measurement chain: sensitivity of the gauges and of the Wheatstone bridges for the tests with the D.T.F.P. used behind the rotor and the second stator in CT3

The maximum length of the probe (L_{MAX}) is adapted to the available space for the measurements in the CT3 facility. Thus, the design of the Vespel support for the probe used in the CT2 facility measurements (see chapter 12) needed to be adapted (Figure 14-1). The length of the probe (L_{MAX}) was shortened from *38* to *23.5mm* (Figure 14-2). Further shortening of L_{MAX} occurred by reducing the length of the ceramic heads, hence the L_{MAX} for the probe behind the rotor is *17.5 mm*.

The sensitivities of the two gauges and of the Wheatstone bridges are given in Table 14-2. A dedicated electronic Wheatstone bridge board is used, similar to the ones used for the heat flux measurements around an airfoil with the single-layer and the two-layer gauges (paragraphs from 4.3.3 till 4.3.6). As there are only two gauges, two channels of the board are used and calibrated. They can operate under two modes (paragraph 4.3.3). In the first mode, called R_0, the overall resistance of the gauge is measured. This is performed just before the blowdown in order to know the initial temperature of the gauges. Note that the calibration of this mode ($R_0 = f(V_0)$ in Table 14-2) needs to be repeated every day before the tests for accurate initial wall temperatures. In the second mode, called ΔR, the Wheastone bridge is balanced in such a way that the output becomes zero for the initial value of the resistance, so that small variations (tenths of millivolts) can be resolved from the data acquisition system. The calibration of the ΔR mode ($d_{\Delta R}/d_{\Delta V}$ in Table 14-2) remains stable for much longer period.

The signal of each gauge is split into two components, one for the time-averaged and one for the time-resolved gas temperature determination (paragraph 4.3.4). The R_0 mode exists only for the time-averaged component. In ΔR mode, the signal is modulated in such a way that the voltage signal of the Wheatstone bridge has a constant amplification as a function of frequency fluctuations up to *100 Hz* and is then amplified by $\sqrt{j\omega}$ between *100 Hz* and *20 kHz*. Above *20 kHz*, the gain decreases. The reason of this modulation is to achieve an adequate resolution of the fluctuations on the *12-bit* data acquisition system. Also note that the time-resolved component is additionally amplified by a constant factor *10*.

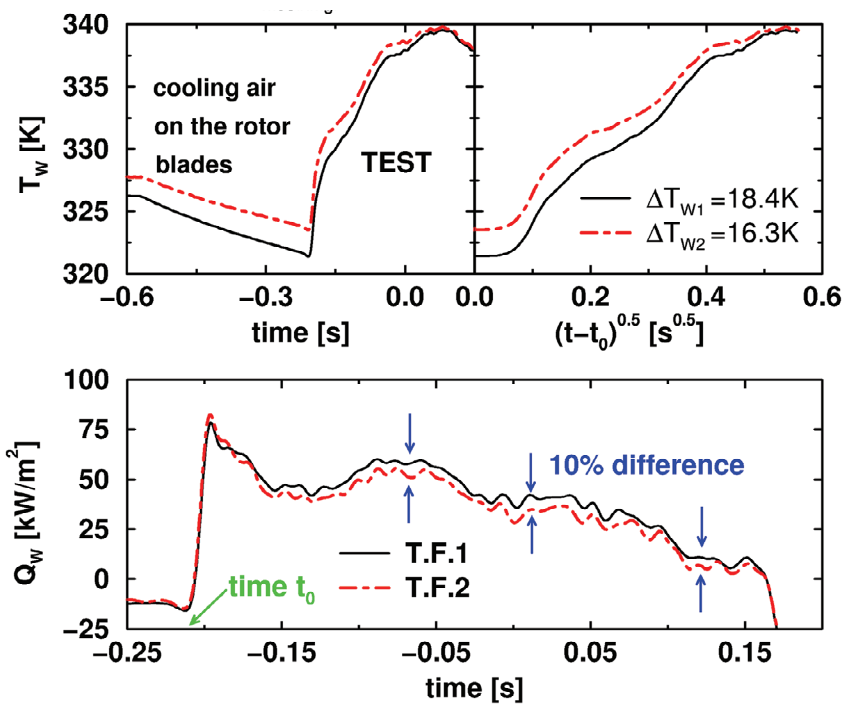

Figure 14-3: Wall heat fluxes during calibration of the D.T.F.P. in CT3 (L_{MAX} = 17.5mm)

The shortest probe (L_{MAX} = *17.5 mm*) is exposed to the flow behind the rotor, when the heating is not activated in order to test if the ratio of the two thermal products is also for this specific probe equal to one. Assuming that the ratio of the two thermal products is equal to one, the wall heat fluxes are given in the bottom graph of Figure 14-3 and a difference of *10%* is observed between the two values of heat flux. The reason of this difference is the initial wall temperature difference between the two gauges (left-top graph) and not any difference between the two thermal products.

More into detail, just prior to the blow down (time from *-0.6s* till *-0.22s*), air that simulates the blade cooling during the test starts running from the blade cooling holes and creates a difference of *2K* on the initial wall temperatures. Thus, the wall temperature change during the test for the thin film sensor 1 (ΔT_{W1}) is *18.4 K* compared to the sensor 2 (ΔT_{W2}), which is *16.3K* (*10%* difference). If the test is approximated as a step in wall heat flux for each head, then each wall temperature rise as a function of square root of time (right-top graph) could be considered proportional to its corresponding wall heat flux (Schultz and Jones, 1973) (see also paragraph 3.3.2). Thus, the *10%* difference on the two values of heat flux results from the *10%* difference on the two values of the wall temperature rise and not from any difference on the two thermal products. (Also note that at time *-0.6s*, the rotor has already started to accelerate and heats up the gauges till not exactly the same temperature.)

14.3 Measurements in CT3 behind the rotor

14.3.1 Time-averaged component

The wall temperature histories are monitored and shown in the first graph of Figure 14-4 for a test performed behind the rotor with the Vespel support probe. The sampling frequency is *1.2 kHz* and the temperature signals are low pass filtered at *90Hz*. (Note that the time which is indicated with negative values, corresponds to the time needed from the flow in CT3 facility to obtain 'relatively constant conditions'. The 'flow establishment' is expected around the time *t=0*.) The gas temperature is calculated and shown in the second graph and it is compared with the thermocouple results, while in the third graph, the wall heat flux histories for each hemispherical head are also presented. Please, note that the temperature peak at the beginning of the test (time from *-0.2s* till *-0.16s*) is *80K* higher than the average gas temperature value during the rest of the test. Porreca and Denos (2002) calculated the total temperature history in the settling chamber of CT3 (T_{01}). The temperature peak reaches *600K*, while during the establishment of the flow the gas temperature is *475K*. Assuming an isentropic efficiency of the first stage (total to total conditions) of *0.9*, the T_{03} peak is calculated equal to *450K* and the T_{03} during the flow establishment is *360K*. These values are very close to the measured ones by the dual thin film probe.

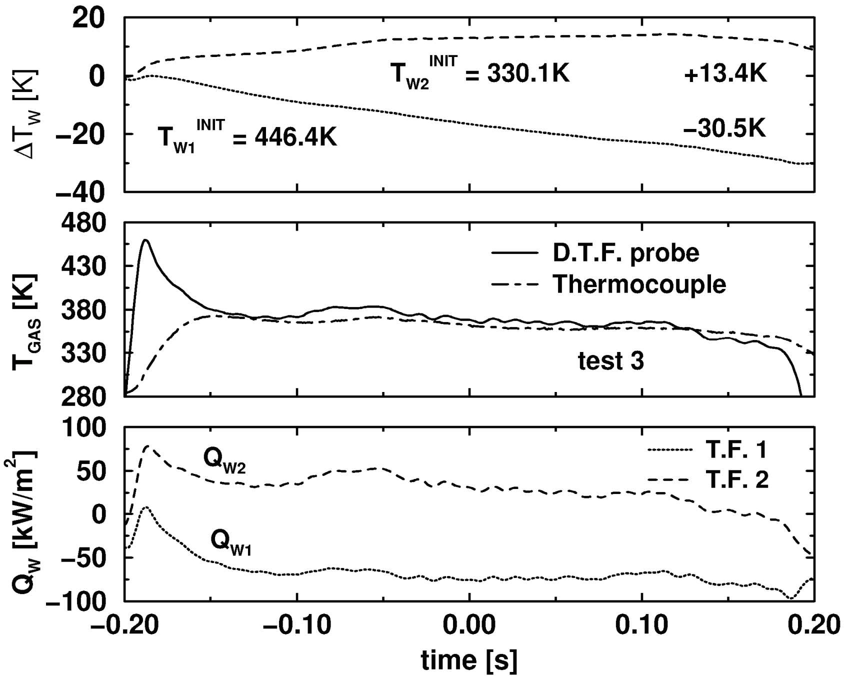

Figure 14-4: Wall temperatures, gas temperature calculations compared to thermocouple and corresponding wall heat fluxes (position: behind the rotor, L_{MAX} = 17.5mm)

In Figure 14-5, three repeatable tests with respect to the one of Figure 14-4 are shown. The thermocouple seems to have reached the real flow conditions around time *-0.15s.* (The time at which the total temperature values measured by the thermocouple reached the values calculated by the probe.) From the tests both in the CT2 facility (see chapter 0) and the CT3 facility, the advantage of the dual thin film probe to detect such high temperature differences that occur in only few milliseconds should be definitely emphasized.

The repeatability of the four tests is demonstrated in Figure 14-6, by plotting all the gas temperature measurements performed by the probe in the same graph (on top). The beginning of the blow down slightly differs from test to test, however, both, the peak and the mean value of the gas temperature seem to be very repeatable. In the top right graph, the difference of the initial wall temperatures is also shown as a function of the one of the hot head (T_{W1}^{INIT}). Although the heating of the ceramic heads is slightly different from test to test, the repeatability of the heat transfer coefficient (*h*) determined by the gauges is evident (bottom graph). (This *h* determination results from Eq. (44), once the gas temperature (T_{GAS}) is substituted from one of the two relationships.) Please note that the heat transfer coefficient calculated by the wall heat fluxes and the wall temperatures contains information not only of the flow (convection), but also of the heating (conduction through the stem of the probe from the hot to the cold head) and thus the initial wall temperatures. This will be discussed is in Chapter 15.4.

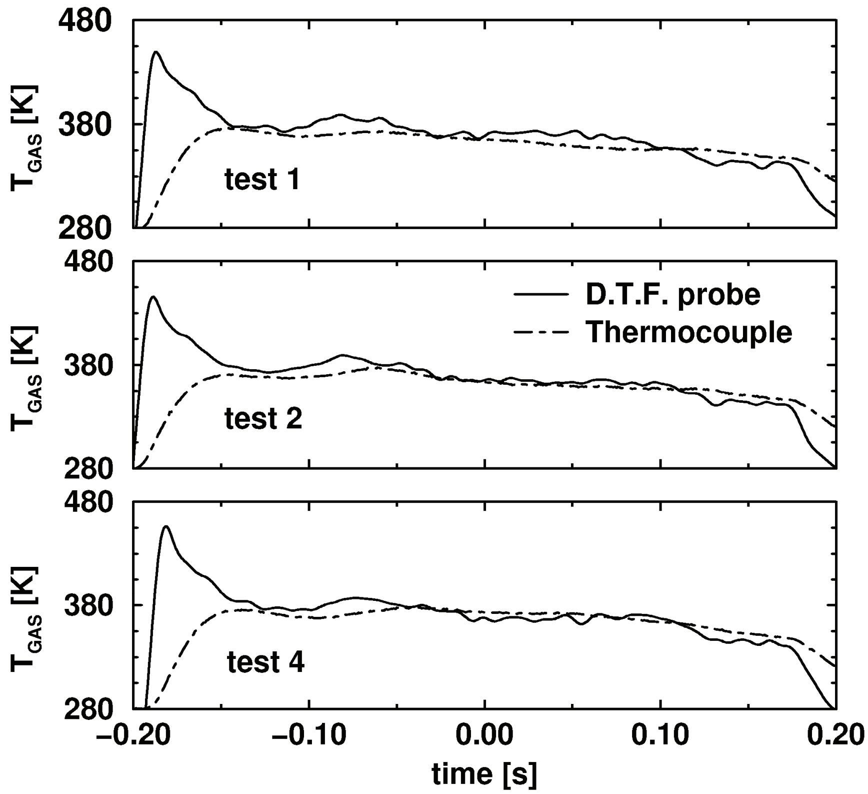

Figure 14-5: Comparison of the gas temperature between the D.T.F. P. and the thermocouple for three repeatable tests behind the rotor of CT3 (L_{MAX} = 17.5mm)

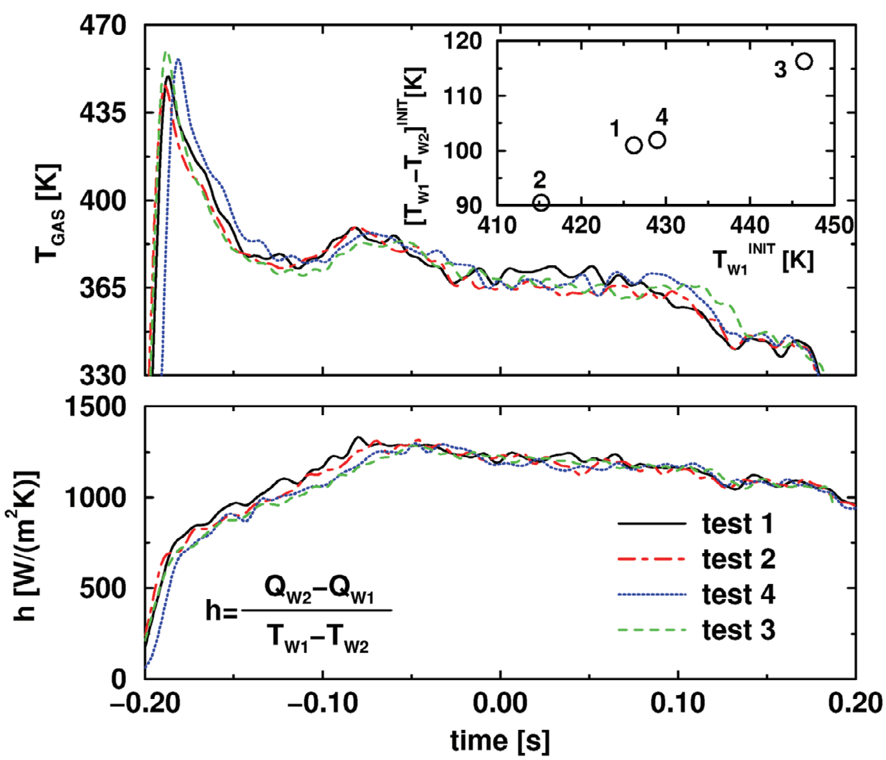

Figure 14-6: Repeatability on the gas temperature measurements performed by the D.T.F.P. and on the heat transfer coefficient (position: behind the rotor, L_{MAX} = 17.5mm)

The repeatability of the determination of the heat transfer coefficient h is reinforced by plotting the wall heat fluxes and their ratio for all the tests (Figure 14-7). The initial wall temperature of the cold ceramic head seems to be for all the tests around *327K* and thus, the equivalent wall heat flux does not really differ from test to test. It is mainly the initial wall temperature of the hot ceramic head that is influenced by the higher heating. This difference on the initial wall temperature is reflected on the wall heat flux. Note that, the ratio of the two heat fluxes has the same contour for all the four tests.

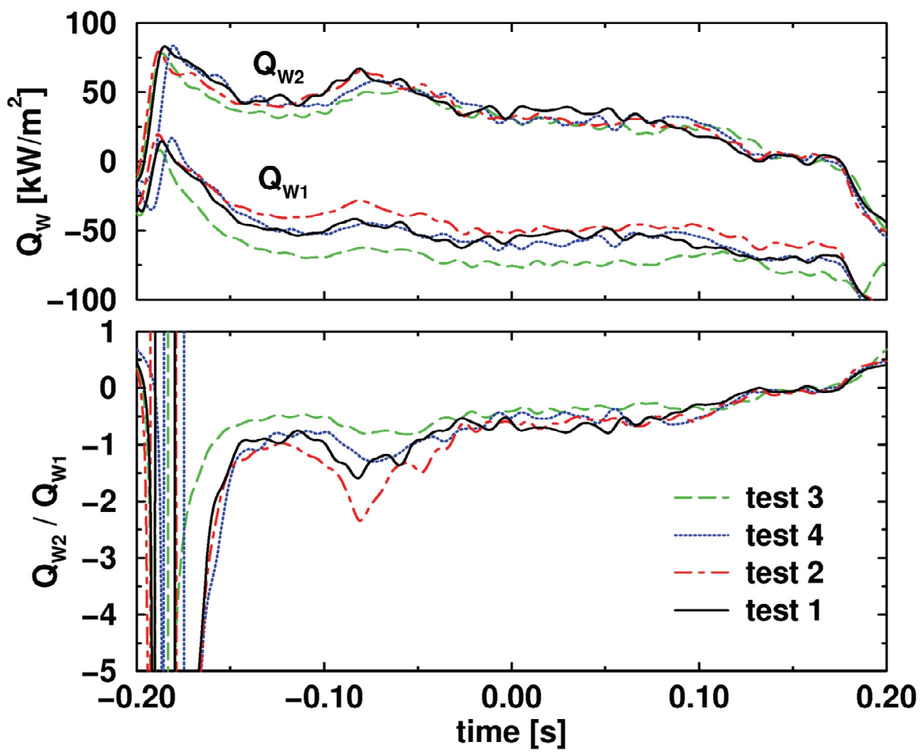

Figure 14-7: Wall heat fluxes and their ratio for four repeatable tests (position: behind the rotor, L_{MAX} = 17.5mm)

14.3.2 Time-resolved component

14.3.2.1 Important parameters and data reduction

The sampling frequency is *300 kHz* and the signal is high pass filtered at *750 Hz* to remove the mean value. The blade passing frequency is *6.9 kHz* at time 0 (Figure 14-4); the evolution of the rotational speed is linear with time and when the nominal peripheral speed of the rotor (*6500 RPM*) is almost reached, the shutter opens. Note that there are *64* blades on the rotor and *10* rotor revolutions are used for the Phase Locked Average (PLA) results. Hence, the total number of periods is *640*. Note that the signal is also amplified as a function of $10\sqrt{j\omega}$ (see paragraphs 4.3.4 and 4.3.5).

First the demodulated voltage signal is transformed to wall temperature fluctuations (step *1* in the post processing chart shown in Figure 14-8). A PLA is performed on these temperature fluctuations based on the rotor blade passing frequency (step *2*). During the step *3*, the PLA temperature fluctuations are transformed from a function of blade passing events (Φ_{rotor}, that is the non-dimensional phase of the rotor blade over a blade period) back to time, and consequently the wall heat flux fluctuations can be calculated (step *4*). After that, both the wall temperature and the heat flux fluctuations are added to their time-averaged component respectively (step *5*). The final wall temperatures and heat fluxes are now used for the gas temperature determination by applying Eq. (45).

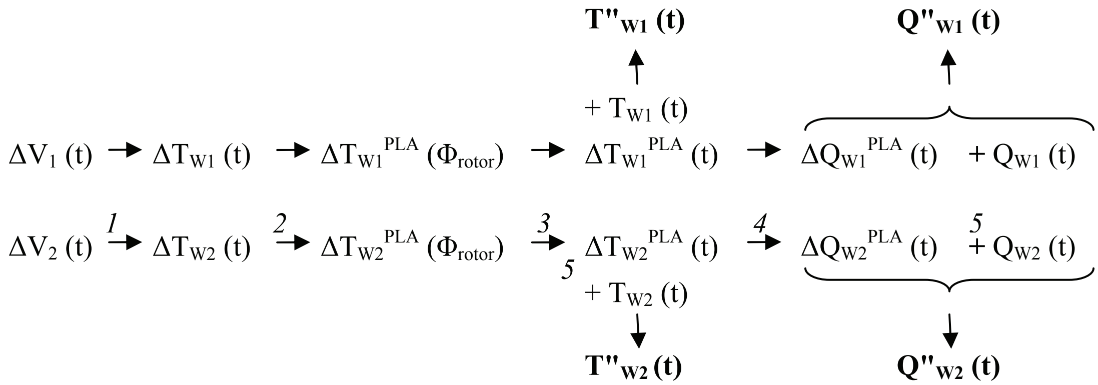

Figure 14-8: Post processing chart for the time-averaged component

14.3.2.2 Periodicity of the raw signal

The Fast Fourier Transformation (FFT) of the demodulated wall temperature of the cold head is shown in Figure 14-9. The resolution in frequency is *18.31 Hz* and the signal is high pass filtered at *750 Hz*. The first harmonic of the blade passing frequency (the probe behind the rotor feels the rotor blades to pass with a frequency of *6.9kHz*, see paragraph 4.4.3.1) is clearly visible as well as the second one. However, there are several frequencies between *1* and *2.5kHz* whose amplitude seems to be important compared to the blade passing frequency.

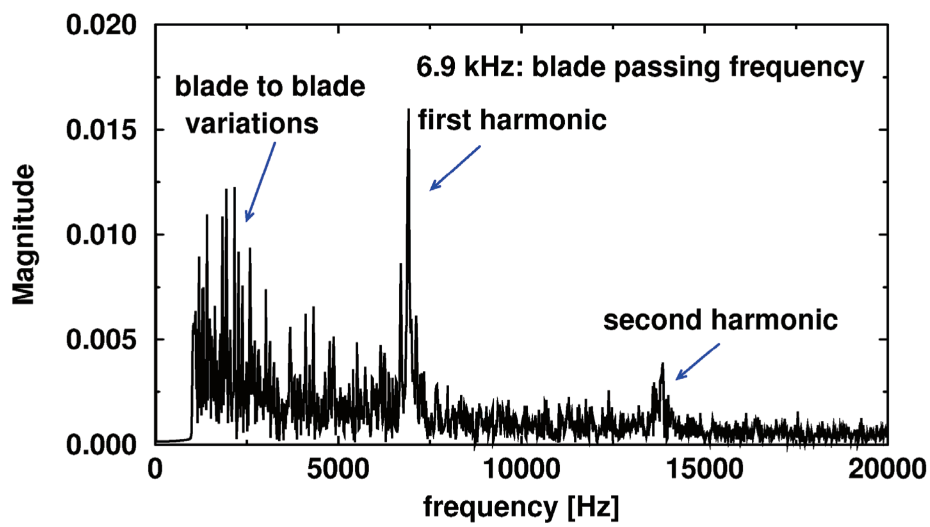

Figure 14-9: FFT on the demodulated wall temperature of the cold head for test 2 (position: behind the rotor, L_{MAX} = 17.5mm)

The high frequency values around *2kHz* are observed for both heads, when the two spectral analysis are plotted on the top of each other (top graph) in Figure 14-10. In the bottom graph, a zoom at frequencies between *1* and *7kHz* of the top graph is shown and demonstrates clearer the frequencies where the highest magnitude is detected, by numbering them from 1 till 13. In Table 14-3, these frequencies (second line) that correspond to the numbering from 1 till 13 (first line) are given together with their multiples of the rotor revolution at *108 Hz* (third line). This analysis strengthens the idea that these frequencies around *2 kHz* are generated by blade to blade variations on the rotor.

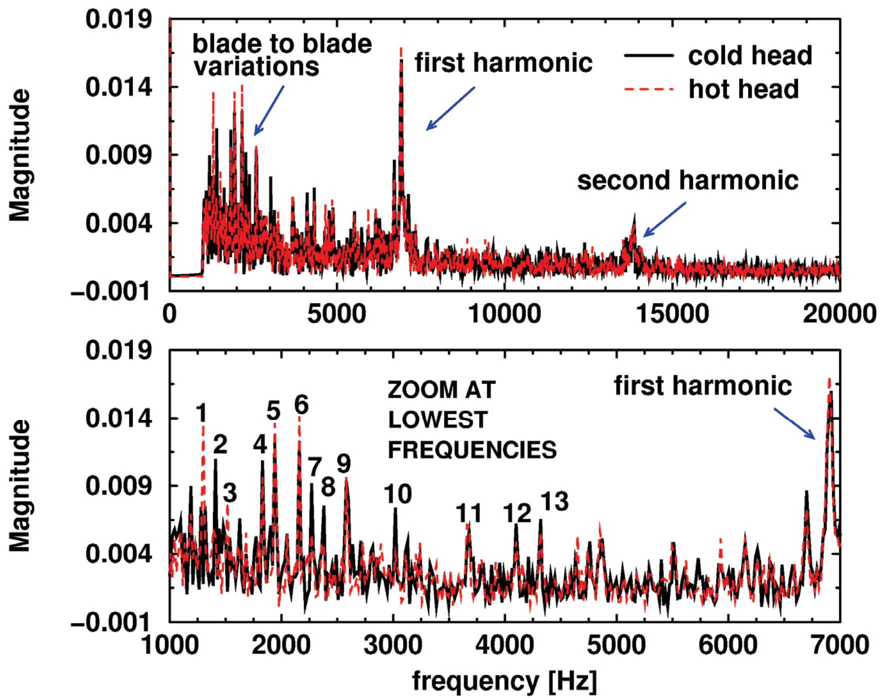

Figure 14-10: FFT on the demodulated wall temperatures for both heads (top) and zoom at frequencies around 2 kHz (bottom) (position: behind the rotor, L_{MAX} = 17.5mm)

No	1	2	3	4	5	6	7	8	9	10	11	12	13
kHz	1.30	1.42	1.52	1.84	1.94	2.16	2.27	2.38	2.59	3.02	3.68	4.10	4.32
/ 108	12.0	13.1	14.1	17.0	18.0	20.0	21.0	22.0	24.0	28.0	34.1	38.0	40.0

Table 14-3: The multiples of the rotor revolution (third line) observed frequencies (second line) during the FFT on the demodulated wall temperatures for both heads behind the rotor

More specifically, the high frequencies around *2kHz* can not be caused by any mechanical movement of the probe as the latter was at fixed position behind the rotor. Also, the mechanical resonance of the probe is expected to be seen if existing at a few Hertz only.

Moreover, the vortex shedding frequency behind the rotor blade trailing edge (f_V) is expected to be either at *25.9 kHz* if the Strouhal number ($St = f_V D/V$) is equal to *0.21* (corresponding to cylinders), or f_V = *32 kHz* if $St = 0.26$ (corresponding to turbulent boundary layers on both pressure and suction sides (Sieverding et al., 1999)). The thickness of the blade trailing edge is *1.3 mm*. Even if only one side of the vortex sheet is taken into account (thus f_V = *12.9* or *16 kHz*), still these high frequency values are far from the area around *2 kHz*. Thus, the origin of these frequencies around *2 kHz* can not be the vortex shedding from the rotor blades.

Last but not least, no aliasing is expected as the sampling frequency is *300 kHz* and the signal is low pass filtered during the test at *40 kHz*.

Miller et al. (2003) describe the blade to blade variations as the vane signature. A spectral analysis was performed on measurements with fast-response pressure transducers on the rotor blades of the Oxford turbine stage facility; frequencies multiple of the rotor revolution and lower than the vane passing frequency (the frequency that the pressure transducers see the vanes of the upstream stator 'passing', if the transducers are considered fixed on the relative rotor frame) were found and attributed to the small blade to blade variations that result in a relatively large variation in the vane exit shock (the operation of the stator was transonic: the exit Mach number was *0.95*).

Consequently, the frequencies around *2 kHz* of the FFT of the two heads signals of the dual thin film probe are also attributed to blade to blade variations (Figure 14-10). Miller et al. (2003) indicate a magnitude for their vane signature frequencies less than four times smaller than the first harmonic of the vane passing frequency. In our case, the rotor signature frequencies are more than half in magnitude of the first harmonic of the blade passing frequency. However, the distance between the vane and the rotor of Miller et al. (2003) is *0.36* times the vane axial chord ($0.36\ C_{AX,V}$), which is higher than the distance of the stagnation area of the heads of the probe with the rotor ($0.215\ C_{AX,R}$). It seems that as the distance of the instrumented probe from the vanes or rotor blades trailing edge increases, the total temperature and pressure fluctuations due to blade to blade variations weaken faster than the fluctuations due to the rotor trailing edge shock wave in the relative frame. Note that the heat transfer measurements with the single-layer gauges on the second stator showed no high frequencies around *2 kHz* (Figure 4-9). Also cold wire measurements performed at $0.392\ C_{AX,R}$ do not capture any frequencies around *2 kHz* (Paniagua et al., 2001).

14.3.2.3 Phase Locked Average results

In Figure 14-11, the repeatability of the PLA on the wall temperature fluctuations is shown for four different tests. The minimum-maximum differences are *0.04* and *0.08K* respectively for the hot and cold head. In addition, the PLA gas temperature fluctuations are shown in Figure 14-12 as a function of time. (The negative values of time correspond to the time needed from the flow in CT3 facility to obtain 'relatively constant conditions'.) They are determined by the total gas temperature minus the time-averaged component. The minimum-maximum difference of the gas temperature fluctuations is about *24K*.

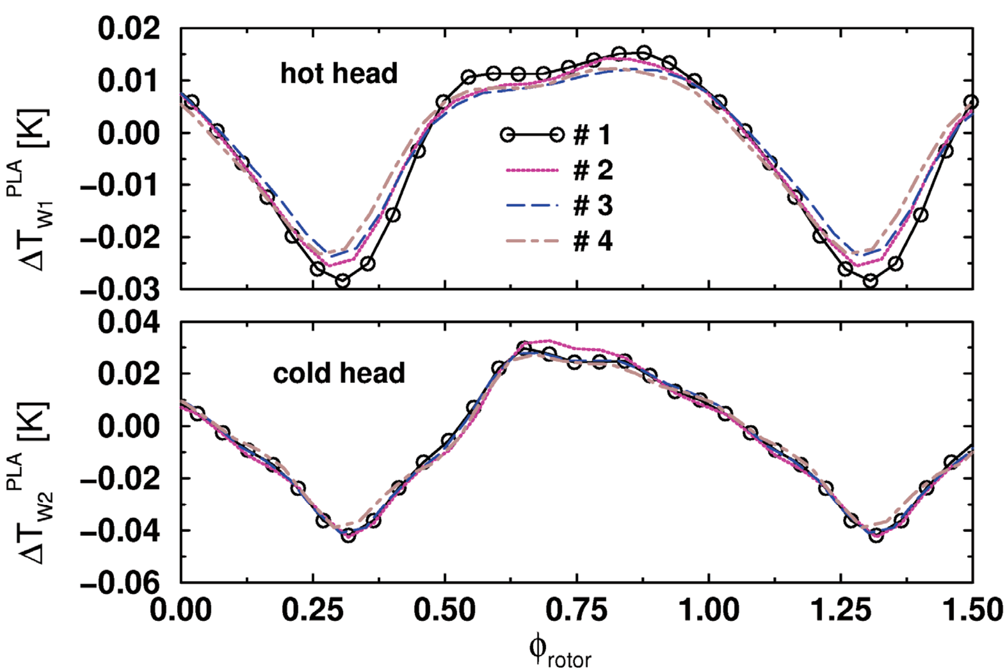

Figure 14-11: Repeatability of the PLA on the two wall temperature fluctuations of the D.T.F.P. (position: behind the rotor, L_{MAX} = 17.5mm)

The average PLA of the gas temperature is compared to the results obtained from cold wire measurements at 43% span in Figure 14-13 (Paniagua et al., 2001). The comparison appears to be satisfactory considering the dimensions of each sensor. The cold wire consists of a *2.5 μm* diameter platinum plated tungsten wire, around one order of magnitude larger than the thickness of the platinum thin films. (The lengths of the thin films and the cold wire are all around *2mm*.) In addition, the two thin film sensors were located at *8.5 mm* downstream of the rotor trailing edge, while the cold wire was at *15.5 mm*, resulting in a possible attenuation of the fluctuations. The gas temperature fluctuations could be originated from the rotor unsteady flow field. There is no dominant steady shock. However, the rotor operates in the transonic regime and instantaneous shocks that create potential flow fluctuations are possible. Thus, the steep total temperature gradient at times just after $-1x10^{-4}s$ and $0.5x10^{-4}s$ (see Figure 14-12) can be an image/trace of the steep static temperature gradient across the shocks at the rotor trailing edge in the relative frame. (Note that the absolute exit Mach number (with an average value of *0.42*) is much smaller than the relative one (with an average value of *0.9*).) It is also possible that these total temperature fluctuations also contain information about the rotor and the first stator wakes. In order to have a definite conclusion on the total temperature fluctuations origin additional measurements on the static temperature or on the absolute exit velocity are necessary. There is only one dominant gas temperature oscillation per rotor blade that implies that the strength of the rotor shock has a stronger influence on the gas temperature fluctuations than the wakes. Also, Paniagua et al. (2001) suggest that the high total pressure fluctuations measured downstream of the rotor could be better explained by the rotor trailing edge shock system, while there was no clear evidence of the rotor wake.

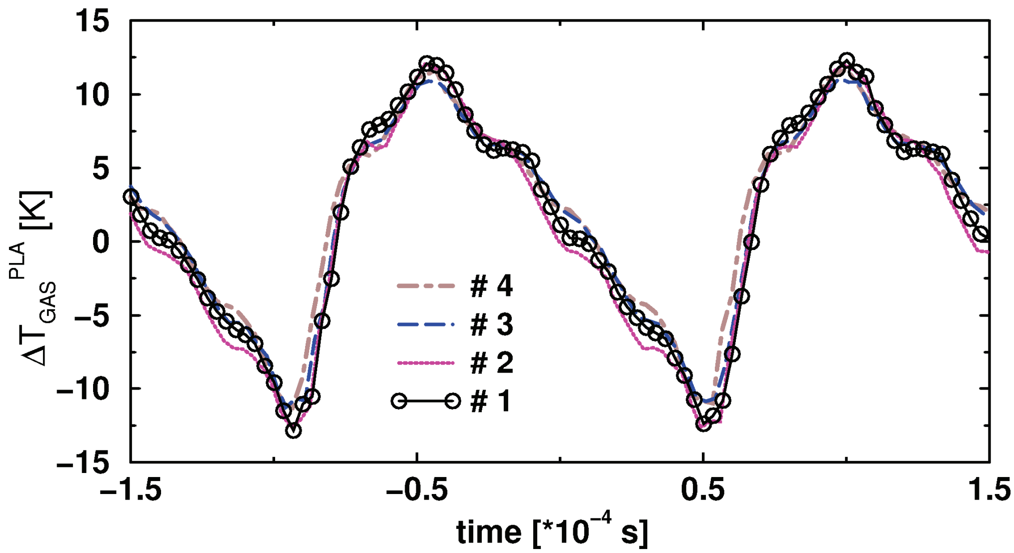

Figure 14-12: Repeatability of the PLA on the gas temperature fluctuations with the D.T.F.P. (position: behind the rotor, L_{MAX} = 17.5mm)

In addition, a comparison between the PLA wall heat flux fluctuations from the two heads is shown on the left graph of Figure 14-14 and the same fluctuations are superposed to the time-averaged component of the wall heat fluxes on the right graph. The amplitude of the wall heat flux fluctuations seems to be half of the magnitude of their steady component. Note that the negative heat fluxes at the beginning of the blowdown (*-0.2 s*) are originated by the cooling flow on the first stator vanes that starts a bit before the shutter opens.

Note that behind each one of the rotor wakes, the flow is three dimensional and the two heads of the probe do not feel exactly the same flow. However, a PLA on the wall temperature signals smoothes out all the non-periodic fluctuations keeping only the mean value of the periodic ones. This is the reason why the mean total temperature fluctuations behind a rotor can be determined with the probe, while the quantification of a single fluctuation of one wake is not possible (see also paragraph 11.4.2)

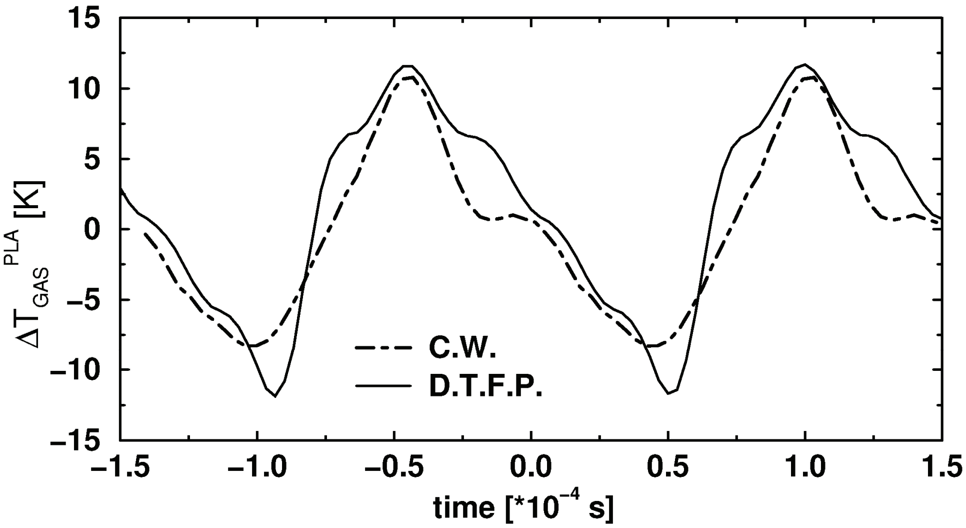

Figure 14-13: Comparison of the PLA on the gas temperature between the D.T.F.P. at midspan and the cold wire at 43% span (position: behind the rotor, L_{MAX} = 17.5mm)

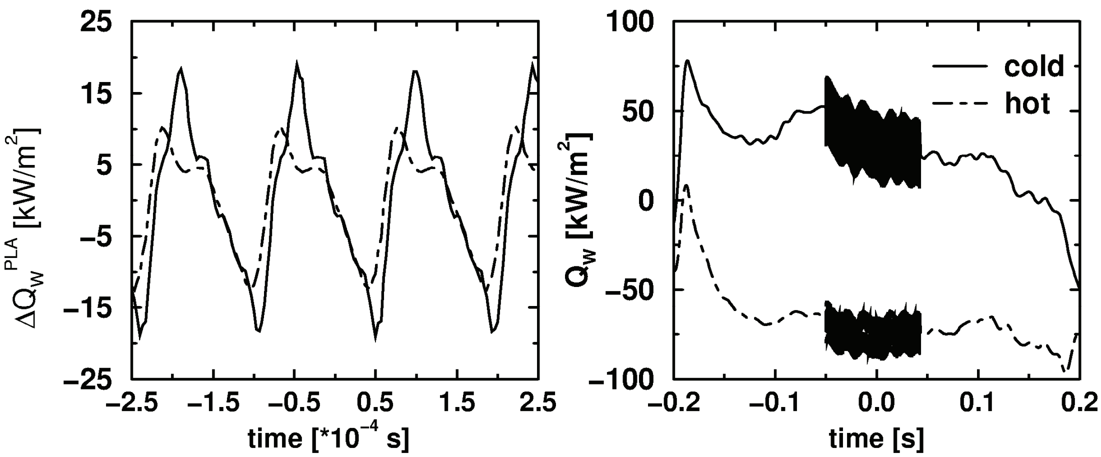

Figure 14-14: The PLA wall heat flux fluctuations and the corresponding final wall heat fluxes in time (position: behind the rotor, L_{MAX} = 17.5mm)

14.4 Measurements in CT3 behind the second stator

14.4.1 Time-averaged component

Compared to the rotor tests (14.3.1), the same data reduction procedure and initial wall boundary choices are followed for the tests behind the second stator of the one and a half stage turbine and the results are mainly compared with the ones of the rotor. Note that the length of the probe used behind the second stator is *23.5mm*. The two wall temperature histories, the corresponding wall heat fluxes and the gas temperature calculation results are shown in Figure 14-15. Three repeatable tests are performed. The time-averaged component of the gas temperature determination is shown in Figure 14-16. The peak at the beginning of the test seems to stay as high as for the measurements behind the rotor. The mean gas temperature during the rest of the test also remains at the same level, as there is no work production in the stator, thus no total temperature drop. However, there is a few Kelvin degrees difference between the two cases, due to the heat transfer on the stator blade walls during the test (non-adiabatic flow close to the walls).

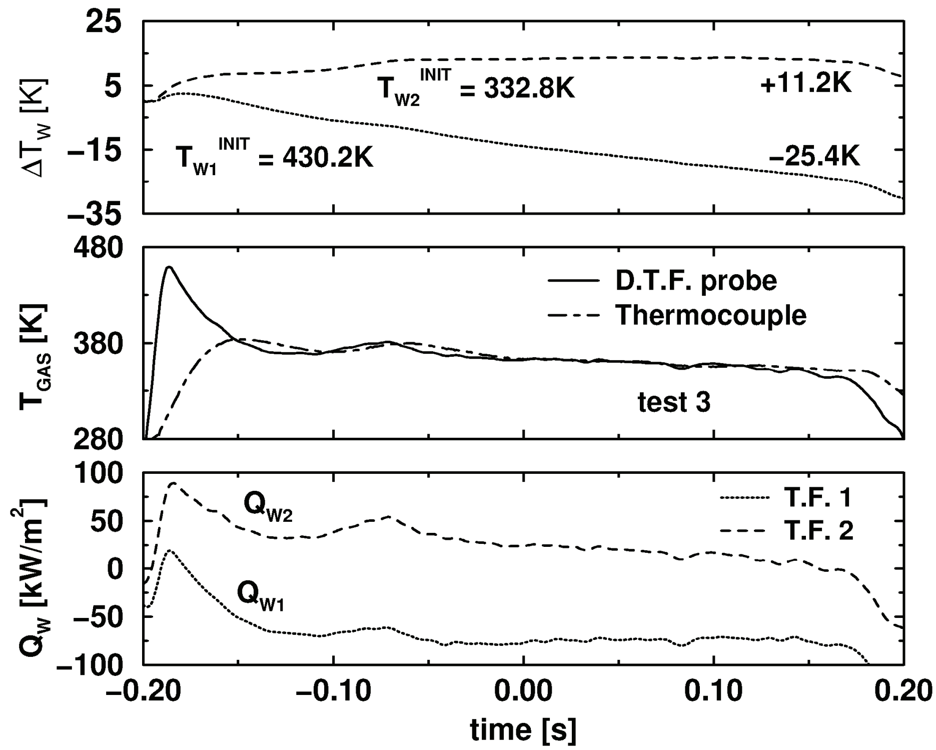

Figure 14-15: Wall temperatures, gas temperature calculations compared to thermocouple measurements and corresponding wall heat fluxes (position: behind the second stator (L_{MAX} = 23.5mm)

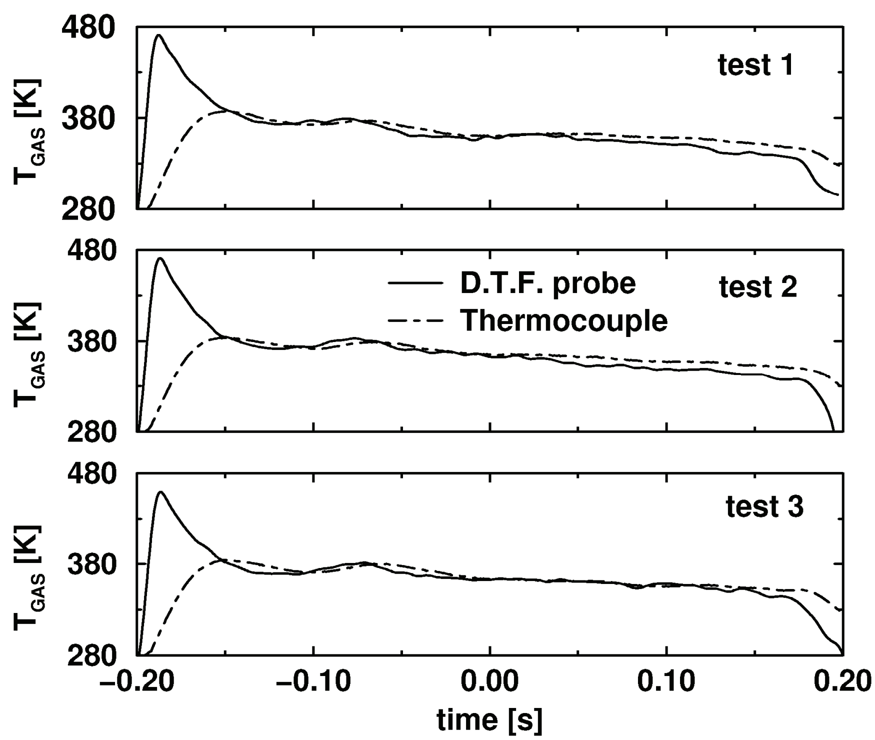

Figure 14-16: Comparison of the gas temperature between the D.T.F.P. and the thermocouple for three repeatable tests (position: behind the second stator, L_{MAX} = 23.5mm)

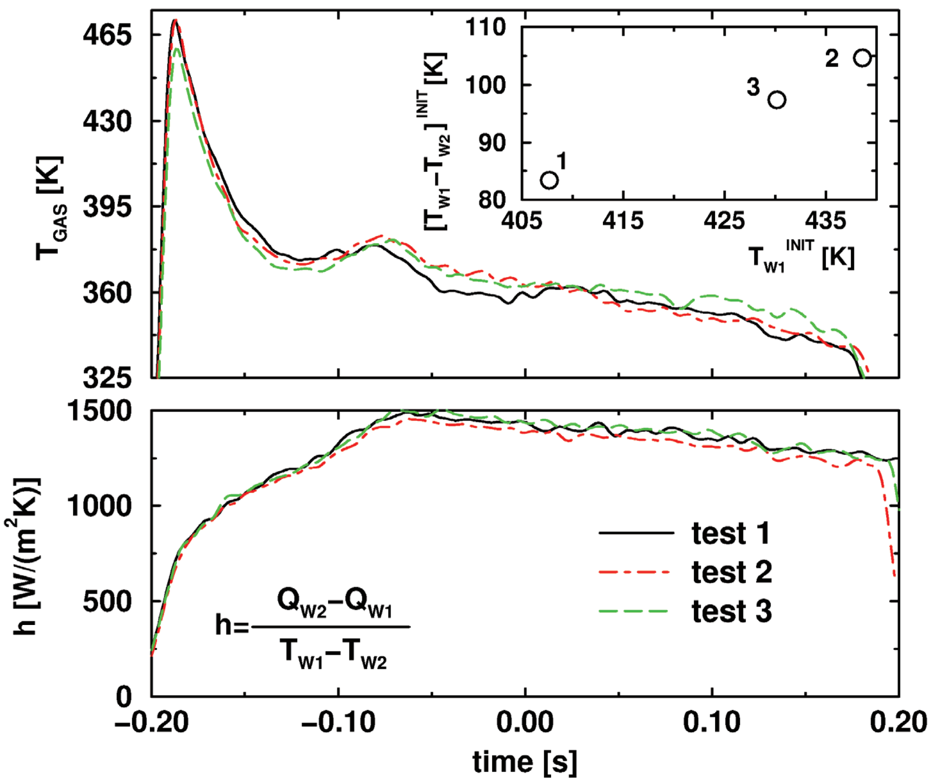

Figure 14-17: Repeatability on the gas temperature measurements performed by the D.T.F.P. and on the heat transfer coefficient (position: behind the second stator, L_{MAX} = 23.5mm)

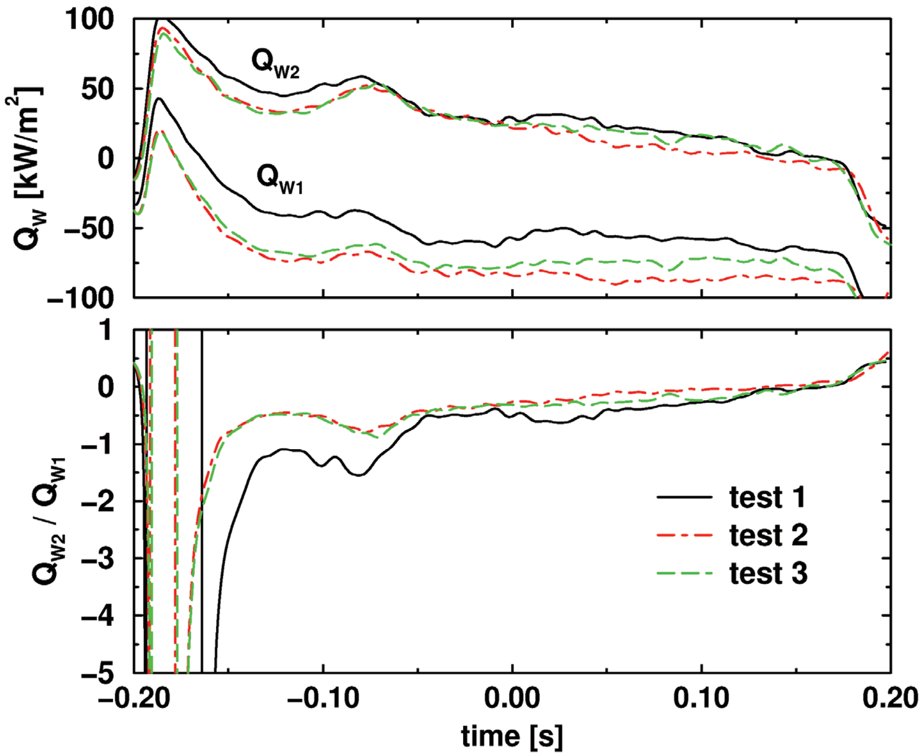

Figure 14-18: Wall heat fluxes and their ratio for three repeatable tests (position: behind the second stator, L_{MAX} = 23.5mm)

The repeatability of the three tests is demonstrated in Figure 14-17, by plotting all the gas temperature measurements performed by the probe on the same graph (top). The difference in heating between the two heads of the probe (right top graph) does not influence the heat transfer coefficient *h* determined by the gauges (bottom graph). This *h* determination results from Eq. (44), once the gas temperature (T_{GAS}) is substituted from one of the two relationships. Please note that the heat transfer coefficient calculation by the wall heat fluxes and the wall temperatures contains information not only of the flow (convection), but also of the heating (conduction through the stem of the probe from the hot to the cold head) and thus the initial wall temperatures. More information is in Chapter 15.4. The repeatability of the determination of the heat transfer coefficient *h* is reinforced by plotting the wall heat fluxes and their ratio for all the tests in Figure 14-7.

14.4.2 Time-resolved component

The PLA on the two wall temperatures as a function of the rotor blade passing events (Φ_{rotor}) and the gas temperature fluctuations are shown in Figure 14-19 and Figure 14-20 respectively for three repeated tests. The fluctuations of both wall temperatures are around *0.002 K*, one order of magnitude below those measured downstream of the rotor (see Figure 14-11), resulting in a *6 K* fluctuation on the total temperature behind the second stator compared to the *24 K* behind the rotor (

Figure 14-12). The mixing of the flow, as it traverses through the stator blade passages seems to be quite high. The probe is fixed in between two stator blades and thus the gas temperature fluctuations (Figure 14-20) are originated:

a) from the unsteady rotor field (corresponding to the big total gas temperature deficit at times between *-0.5* and *0* and between *1* and $1.5x10^{-4}s$),

b) from the first stator wake (corresponding to the small deficit at times around *-1* and $0.5x10^{-4}s$).

The number of the second stator vanes is equal to the number of the first stator vanes (43). When the leading edge of the second stator vanes are aligned with the leading edge of the first stator vanes, the clocking between the two stators is 0 (see Figure 4-4). The first measurement of Figure 14-20 corresponds to clocking 0. The second measurement corresponds to clocking 1 (the position of the second stator is shifted 25% of the vanes pitch to the same direction of the rotation of the rotor blades) and the third measurement corresponds to clocking 2 (a shift of 50% pitch).

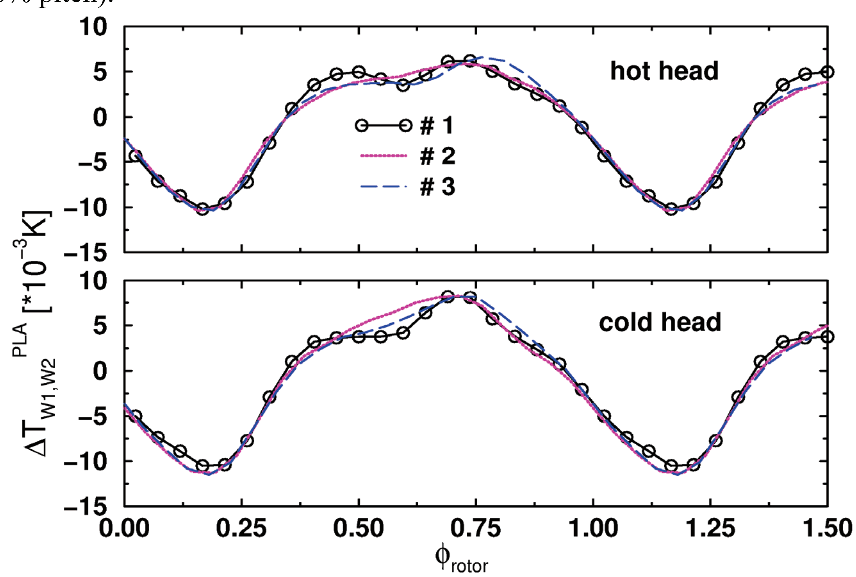

Figure 14-19: Repeatability of the PLA on the two wall temperature fluctuations of the D.T.F. P. (position: behind the second stator, L_{MAX} = 23.5mm)

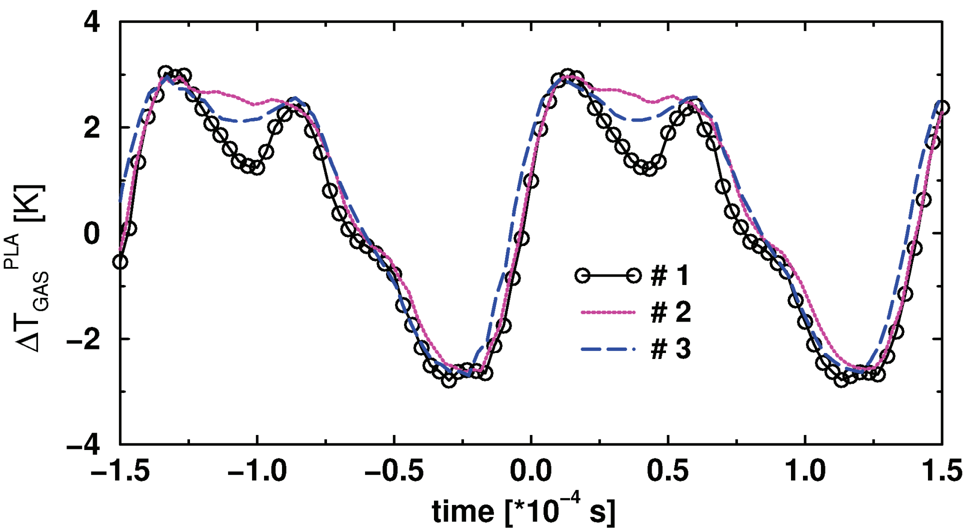

Figure 14-20: Repeatability of the PLA on the gas temperature fluctuations with the D.T.F. P. (position: behind the second stator, L_{MAX} = 23.5mm)

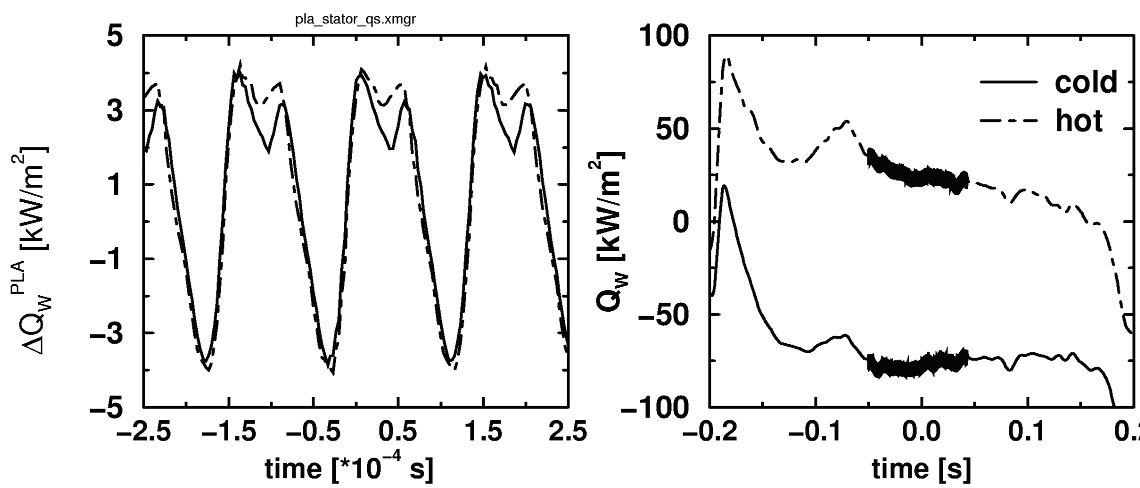

Figure 14-21: The PLA wall heat flux fluctuations and the corresponding final wall heat fluxes in time (position: behind the second stator, L_{MAX} = 23.5mm)

Also, a comparison between the PLA wall heat flux fluctuations from the two heads is shown on the left graph of Figure 14-21 and the same fluctuations are superposed to the time-averaged component of the wall heat fluxes on the right graph. The amplitude of the wall heat flux fluctuations seems to be at least one order of magnitude less than their steady component, as opposed to the measurements behind the rotor (Figure 14-14).

The new design of the probe for the CT3 tests as well as the results from the measurements behind the rotor and the second stator of the VKI one and a half stage turbine are also published by Iliopoulou and Arts (2005).

14.5 References

Denos, R., 1996, *'Aerothermal investigation of the unsteady flow in the rotor of a transonic turbine stage'*, Ph.D. thesis, University of Poitiers, France

Iliopoulou V., Arts T., 2005, '*The dual thin-film probe for high frequency flow temperature measurements'*, Proc. 6th conf. on Turbomachinery, Fluid Dynamics and Thermodynamics, Lille, France – to be published in Proc. of the Institution of Mech. Eng. Part A 'J. of Power and Energy'

Miller R.J., Moss R.W., Ainsworth R.W., Harvey N.W., 2003, *'Wake, shock, and potential interactions in a 1.5 stage turbine – Part I: Vane-rotor and rotor-vane interaction'*, J. of Turbomachinery, Vol. 125, pp33-39

Paniagua G., Denos R., Arts T., 2001, *'Steady-unsteady measurements of the flow field downstream of a transonic high-pressure turbine stage'*, Proc. of the Inst. of Mech Engrs, vol. 215 (A) pp 663-673.

Porreca L., Denos R., 2002, *'Turbine stage mass flow evaluation in a compression tube facility'*, Proc., 16th Symposium on Measuring Techniques, Cambridge, Great Britain

Sieverding, C. H., and Arts, T., 1992, *'The VKI compression tube Annular Cascade Facility CT3'*, ASME paper 92-GT-336, Koln, Germany

Sieverding C.H., Cicatelli G., Desse J.M., Meinke M., Zunino P., 1999, *'Experimental and numerical investigation of time varying wakes behind turbine blades'*, Notes on numerical fluid mechanics vol 67, Results of the Industrial and material technology aeronautics research project AER2-CT92-0048 (1992-1996), ISSN 0179-9614, ISBN 3-528-06967-8, Germany